 doi:10.20944/preprints202011.0705.v1

Enhanced photovoltaic properties of perovskite solar cells by employing bathocuproine/hydrophobic polymer films as hole-blocking/electron-transporting interfacial layers

Guan-Zhi Liu[1], Chi-Shiuan Du[1], Jeng-Yue Wu[1], Bo-Tau Liu[2*], Tzong-Ming Wu[3], Chih-Feng Huang[1], and Rong-Ho Lee[1*]

1. Department of Chemical Engineering, National Chung Hsing University, Taichung 402, Taiwan
2. Department of Chemical and Materials Engineering, National Yunlin University of Science and Technology, Yunlin 64002, Taiwan
3. Department of Materials Science and Engineering, National Chung Hsing University, Taichung 402, Taiwan

*To whom correspondence should be addressed.

Bo-Tau Liu—e-mail: liubo@yuntech.edu.tw; tel.: +886-4-22854308; fax: +886-4-22854734.

Rong-Ho Lee—e-mail: rhl@dragon.nchu.edu.tw; tel.: +886-4-22854308; fax: +886-4-22854734.

 doi:10.20944/preprints202011.0705.v1

Abstract

In this study, we improved the photovoltaic (PV) properties and storage stabilities of inverted perovskite solar cells (PVSCs) based on methylammonium lead iodide ($MAPbI_3$) by employing bathocuproine (BCP)/poly(methyl methacrylate) (PMMA) and BCP/polyvinylpyrrolidone (PVP) as hole-blocking and electron-transporting interfacial layers. The architecture of the PVSCs was indium tin oxide/poly(3,4-ethylenedioxythiophene):polystyrenesulfonate/$MAPbI_3$/[6,6]-phenyl-C_{61}-butyric acid methyl ester/BCP:PMMA or BCP:PVP/Ag. The presence of PMMA and PVP affected the morphological stability of the BCP and $MAPbI_3$ layers. The storage-stability of the BCP/PMMA-based PVSCs was enhanced significantly relative to that of the corresponding unmodified BCP-based PVSC. Moreover, the PV performance of the BCP/PVP-based PVSCs was enhanced when compared with that of the unmodified BCP-based PVSC. Thus, incorporating hydrophobic polymers into BCP-based hole-blocking/electron-transporting interfacial layers can improve the PV performance and storage stability of PVSCs.

Keywords: bathocuproine, methylammonium lead iodide, electron-transporting interfacial layer, perovskite solar cells.

Preprints (www.preprints.org) | NOT PEER-REVIEWED | Posted: 27 November 2020 doi:10.20944/preprints202011.0705.v1

1. Introduction

Organometal halide perovskites, particularly methylammonium lead iodide ($CH_3NH_3PbI_3$, $MAPbI_3$) and methylammonium lead bromide ($CH_3NH_3PbBr_3$, $MAPbBr_3$), are highly suitable for use in solar cells because of their excellent photovoltaic (PV) properties [large absorption coefficients in the Vis to near-infrared (NIR) region, long diffusion lengths of charge carriers, excellent charge mobility, and high photoconversion efficiencies (PCEs)] [1–6]. Perovskite solar cells (PVSCs) having planar or mesoscopic structures can be fabricated through solution processing with thermal treatment at low temperature [6–8]. Many efforts have been made to improve the PV properties of PVSCs; for example, by designing new perovskite materials with high photo-electron conversion [9,10], interfacial engineering between the perovskite layer and the electron- or hole-transporting layer (ETL or HTL) [11–14], controlling the crystal growth of the perovskite [15–20], and adding suitable amounts of halide, cationic, organic, and polymer additives in the perovskite layer [21–29].

In addition to a high PCE, a PVSC must possess high operational stability if it is to find wide applicability [26, 30]. Incorporating an inorganic material [27, 28] or hydrophobic polymer under the cathode layer can be an effective method to protect the PVSC from the permeation of oxygen and humidity [29]. For example, hydrophobic poly(methyl methacrylate) (PMMA) has been incorporated into PVSCs to enhance their operational and storage stabilities [30–33]. Kundu et al. reported a PVSC featuring an HTL comprising of poly(3-hexylthiophene) (P3HT) and PMMA; the PMMA matrix imparted good resistance to the permeation of moisture, resulting in a large enhancement of the stability of the cell [30]. Habisreutinger et al. found that depositing PMMA on top of a P3HT/single-walled carbon nanotube (SWNT) nanohybrid–based HTL filled the voids within the P3HT/SWNT nanohybrid and blocked the contact of the Ag-based cathode with the $MAPbI_3$ layer; incorporating the

Preprints (www.preprints.org) | NOT PEER-REVIEWED | Posted: 27 November 2020 doi:10.20944/preprints202011.0705.v1

PMMA layer enhanced the shunt resistance, open-circuit voltage (V_{OC}), and fill factor (FF) of the PVSC, while also inhibiting the permeation of moisture into the $MAPbI_3$ layer and increasing the storage stability [32]. Furthermore, adding PMMA into two-dimensional layered $MAPbI_3$ intermediates has led to self-assembly into three-dimensional perovskite crystal grains featuring a coating of PMMA at the crystal grain boundaries; this bilayer structure inhibited the permeation of moisture and enhanced the stability of $MAPbI_3$ [33]. Moreover, the presence of a PMMA film can decrease the trap density by compensating electronically for iodide vacancies along the boundary; this approach can minimize charge recombination and improve the values of V_{OC} of PVSCs [33].

In addition to PMMA, the hydrophobic polymer polyvinylpyrrolidone (PVP) has also been used as an interfacial material between the ETL and the cathode to improve PV performance. The quality of the ETL–cathode interface can have a dramatic effect on the electron transport and extraction in the PVSC. Incorporating PVP has promoted electron transport across the perovskite–cathode interface when using a [6,6]-phenyl-C_{61}-butyric acid methyl ester ($PC_{61}BM$)–based ETL. Moreover, the presence of a dipole layer after the addition of PVP can enhance the built-in potential across the cell, thereby favoring charge transport from the ETL to the cathode and improving the PV properties [34]. In addition, hydrophobic PVP has been used as an additive in the perovskite layer to improve PV performance by protecting the perovskite crystals from the damaging effects of moisture; the acylamino groups of PVP enhanced the electron density at the perovskite surface and, thereby, decreased the surface energy and stabilized the perovskite layer; the resulting PVSC displayed a high PCE and excellent moisture-stability [35]. Furthermore, strong interactions between Pb(II) ions and the C=O groups in PVP can lead to the nuclei distributing uniformly along the PVP chains, resulting in compact $MAPbI_3$ films; consequently, PVP-added perovskite layers can

Preprints (www.preprints.org) | NOT PEER-REVIEWED | Posted: 27 November 2020 doi:10.20944/preprints202011.0705.v1

possess crystalline structures that enhance the PCE-stability of their PVSCs [36–39].

In inverted PVSCs, the fullerene derivative $PC_{61}BM$ is usually employed as an electron extraction layer and ETL at the perovskite–cathode interface. Introducing a bathocuproine (BCP)-based hole-blocking/electron-transporting interfacial layer between the $PC_{61}BM$ layer and the cathode can enhance a PVSC's FF and short-circuit current density (J_{SC}) by filling voids and improving the surface morphology of the $PC_{61}BM$ layer [6,40]. The polar functional groups of BCP can enhance the value of V_{OC} of a PVSC by effectively enhancing its built-in potential [41]. Moreover, the presence of BCP prevents Ag atoms from diffusing from the cathode to the $MAPbI_3$ layer, thereby enhancing the operational stability of the PVSCs [42]. In this present study, we measured the PV properties and storage stabilities of $MAPbI_3$-based inverted PVSCs incorporating BCP/PMMA and BCP/PVP composites as their hole-blocking/electron-transporting interfacial layers. The architecture of our PVSCs (Figure 1) was indium tin oxide (ITO)/poly(3,4-ethylenedioxythiophene):polystyrenesulfonate (PEDOT:PSS)/$MAPbI_3$/$PC_{61}BM$/BCP:PMMA or BCP:PVP/Ag. Incorporating PMMA into the BCP layer enhanced the storage stability of our PVSC, while PVP in the BCP layer facilitated electron transport at the perovskite–cathode interface. We used scanning electron microscopy (SEM) and X-ray diffractometry (XRD) to examine the morphologies and crystal structures of the resulting perovskite layers, and atomic force microscopy (AFM) to observe the morphologies of the BCP/PMMA and BCP/PVP layers. The hydrophobicity/hydrophilicity of the BCP/PMMA and BCP/PVP layers were determined using a contact angle (CA) meter. We found that the BCP/PMMA and BCP/PVP interfacial layers enhanced the PV properties, the PCEs, and the storage stabilities of their $MAPbI_3$-based PVSCs.

Preprints (www.preprints.org) | NOT PEER-REVIEWED | Posted: 27 November 2020 doi:10.20944/preprints202011.0705.v1

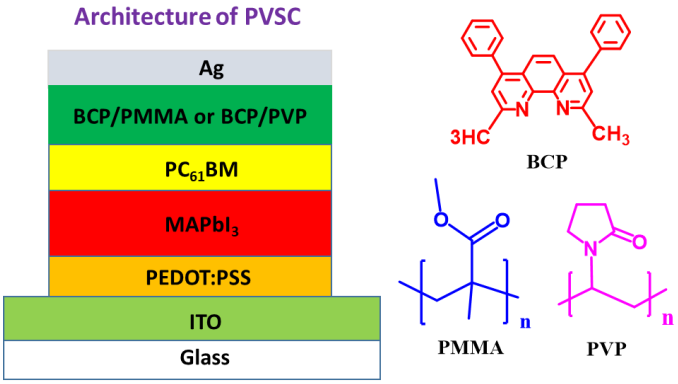

Figure 1. Architecture of the inverted PVSCs.

2. Experimental Details

2-1 Materials and Instrumentation

Methylamine (CH_3NH_2), lead iodide (PbI_2), BCP, PMMA (M_w = 15,000), and PVP (M_w = 10,000) were purchased from Sigma–Aldrich, Acros, and TCI Chemical, and used without purification. $PC_{61}BM$ was purchased from NANO-C. Isopropanol, γ-butyrolactone (GBL), dimethylsulfoxide (DMSO), toluene, and *o*-dichlorobenzene (*o*-DCB) were distilled over appropriate drying agents prior to use.

Fourier transform infrared (FTIR) spectra were recorded using a HORIBA FT-720 FTIR spectrometer. Differential scanning calorimetry (DSC, TA Instruments, DSC-2010) was used to determine the glass transition temperatures (T_g) of the BCP/PMMA and BCP/PVP blend films under a N_2 atmosphere (scanning rate: 10 °C min^{-1}). UV–Vis absorption spectra were recorded using a Hitachi U3010 UV–Vis spectrometer. Photoluminescence (PL) spectra were recorded using a Hitachi F-4500 fluorescence spectrophotometer. AFM images of BCP/PMMA and BCP/PVP blend films coating the surface of the ETL ($PC_{61}BM$) were recorded using a Seiko SII SPA400 atomic force microscope operated in tapping mode. Cold field emission scanning electron microscopy (FESEM) images of the $MAPbI_3$ layer were recorded using a Hitachi S-4800 microscope. Powder XRD of the perovskite layer was measured using a Shimadzu SD-D1 instrument and a Cu target. The CAs of water droplets on the

Preprints (www.preprints.org) | NOT PEER-REVIEWED | Posted: 27 November 2020 doi:10.20944/preprints202011.0705.v1

BCP/PMMA and BCP/PVP films were determined using a Kyowa DropMaster optical CA meter.

2.2 Fabrication and Characterization of PVSCs

The architecture of the PVSCs was ITO-coated glass/PEDOT:PSS/$MAPbI_3$/$PC_{61}BM$/BCP:PMMA or BCP:PVP/Ag (100 nm). The photoactive area of each device was 0.24 cm^2. ITO-coated glass having a sheet resistance of 20 Ω $square^{-1}$ was obtained from Luminescence Tech; $PC_{61}BM$ was procured from Nanocarbon. The glass substrates featuring patterned ITO electrodes were washed well and then cleaned using O_2 plasma. PEDOT:PSS (AI4083, Heraeus Clevios) was spin-coated onto the ITO layer. The sample was heated at 110 °C for 30 min. Methylammonium iodide (MAI; 0.200 g, 1.25 mmol) and PbI_2 (0.580 g, 1.25 mmol) were stirred in a mixture of GBL and DMSO (1:1, v/v; 1 mL) to obtain a $MAPbI_3$ solution. The $MAPbI_3$ solution (0.2 mL) was deposited on the surface of PEDOT:PSS layer through two consecutive spin-coating processes at 1000 and 3000 rpm for 10 and 30 s, respectively. During the second spin-coating process, toluene (0.5 mL) was drop-cast onto the substrate, which was then dried on a hot plate (80 °C, 5 min). A solution (0.2 mL) of $PC_{61}BM$ (20 mg mL^{-1}) in *o*-DCB was coated on top of the $MAPbI_3$ layer; a solution (0.3 mL) of BCP or a BCP/polymer (PMMA or PVP) blend in isopropanol (0.5 mg mL^{-1}) was then coated on the $PC_{61}BM$ layer. The Ag cathode was thermally deposited onto the BCP/PMMA or BCP/PVP layer under high vacuum. The PV parameters of the PVSCs were determined using a programmable electrometer (Keithley 2400) under illumination with AM1.5 light from a solar simulator (NewPort Oriel 96000) at an intensity of 100 mW cm^{-2}.

3. Results and Discussion

3.1 Chemical Structures and Thermal Properties of BCP/PMMA and BCP/PVP Blends

Preprints (www.preprints.org) | NOT PEER-REVIEWED | Posted: 27 November 2020 doi:10.20944/preprints202011.0705.v1

The functional groups in the BCP/PMMA and BCP/PVP blends were characterized using FTIR spectroscopy. FTIR spectra of BCP, PMMA, PVP, BCP/PMMA (5:1, w/w), and BCP/PVP (5:1, w/w) are provided in Figure 2. In the spectra of BCP, PMMA, and PVP, the signals for C–H stretching appeared in the range 2300–3200 cm^{-1} and those for C–H bending in the CH_3 and CH_2 units at 1450–1600 cm^{-1}. In the spectrum of BCP, the signal for =C–H bending of the aromatic ring appeared at 707 cm^{-1}; the signal of the imino (C=N) group appeared at 1716 cm^{-1}; and the signals for C=C stretching in the aromatic ring appeared at 1488 and 1569 cm^{-1}. In the spectra of PMMA and PVP, the signals for C=O stretching appeared at 1733 and 1656 cm^{-1}, respectively; for PMMA, the signals for the C–O moieties of the ester groups appeared at 1147 and 1193 cm^{-1}; for PVP, the signal for C–N stretching appeared at 1290 cm^{-1}. Furthermore, the signals of BCP, PMMA, and PVP appeared in the spectra of the BCP/PMMA and BCP/PVP blends.

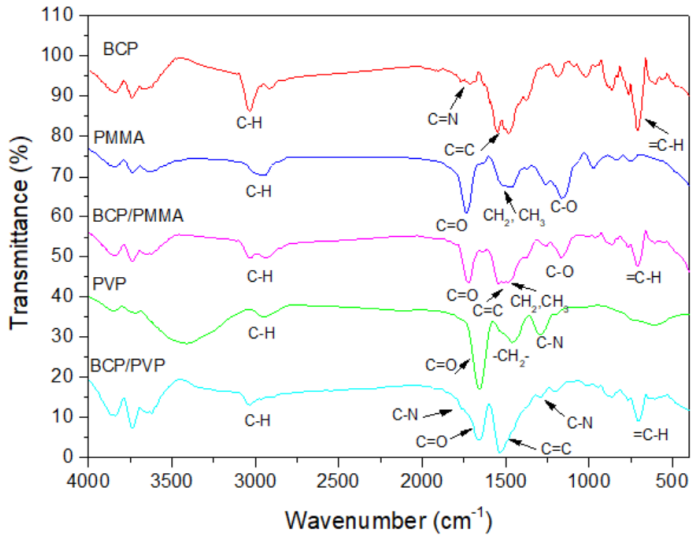

Figure 2. FTIR spectra of BCP, PMMA, PVP, BCP/PMMA (5:1, w/w), and BCP/PVP (5:1, w/w).

Figure 3 displays DSC thermograms of BCP, BCP/PMMA (5:1, w/w), and BCP/PVP (5:1, w/w). The values of T_m for BCP, BCP/PMMA, and BCP/PVP samples were 289, 279, and 283 °C, respectively. The lower value of T_m of the BCP/PMMA

Preprints (www.preprints.org) | NOT PEER-REVIEWED | Posted: 27 November 2020 doi:10.20944/preprints202011.0705.v1

blend implies that its miscibility was greater than that of the BCP/PVP blend.

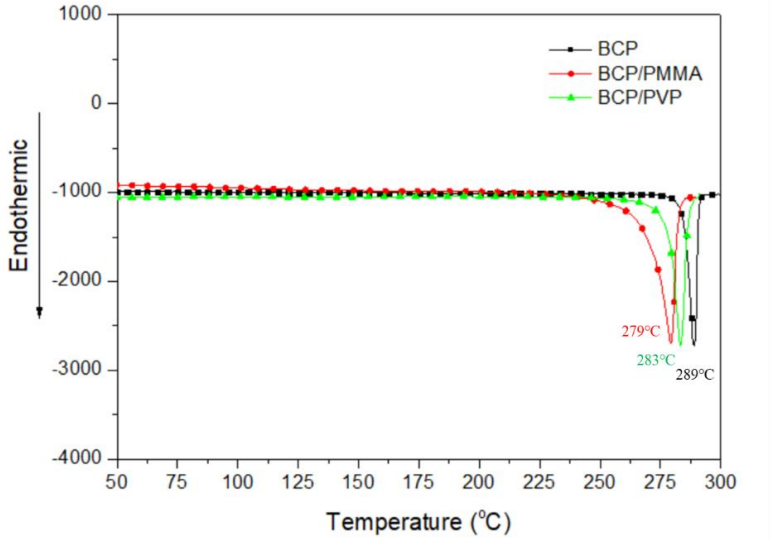

Figure 3. DSC thermograms of BCP, BCP/PMMA (5:1, w/w), and BCP/PVP (5:1, w/w).

3.2 Optical Properties of $MAPbI_3$ Perovskite Film

We recorded UV–Vis absorption and photoluminescence (PL) spectra to examine the optical properties of the $MAPbI_3$ layer (Figure S1). The absorption onset of the $MAPbI_3$ layer (ca. 780 nm) suggested an optical band gap of 1.6 eV [43]. The maximal PL wavelength of the $MAPbI_3$ layer appeared near 768 nm, when excited at a wavelength of 510 nm [44].

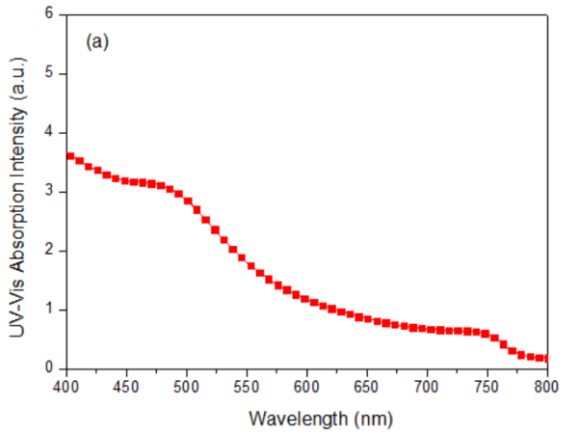

Preprints (www.preprints.org) | NOT PEER-REVIEWED | Posted: 27 November 2020 doi:10.20944/preprints202011.0705.v1

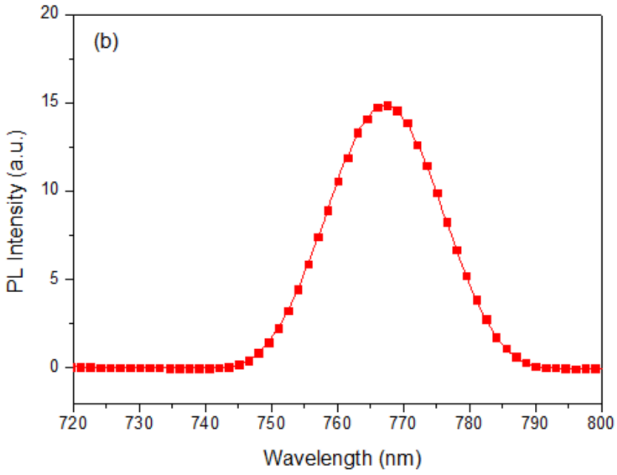

Figure S1. (a) UV–Vis absorption and (b) PL spectra of the $MAPbI_3$ perovskite film.

3.3 SEM Images of $MAPbI_3$ Layers Coated with Various Electron-Transporting Interfacial Films

Figure 4 presents SEM images of the $MAPbI_3$ perovskite film. In addition to the presence of grain boundaries between crystals, the crystal grains were distributed uniformly in the $MAPbI_3$ perovskite film, without other defects. The largest crystal grain had a size of approximately 210 nm. Such a high-quality $MAPbI_3$ layer is generally favorable for PVSCs displaying high PV performance. Figure 5 displays cross-sectional SEM images of ITO/PEDOT:PSS/$MAPbI_3$/$PC_{61}BM$ structures coated with electron-transporting interfacial layers of BCP, BCP/PMMA, and BCP/PVP films. The thicknesses of the $MAPbI_3$ layers ranged from 275.6 to 290.6 nm. We suspected that the dense packing of the grain crystals of the $MAPbI_3$ layer would minimize grain boundary defects and enhance the charge transfer capacity. These $MAPbI_3$-based photoenergy conversion layers possessed good film quality. In addition, the thicknesses of the $PC_{61}BM$/BCP/polymer (PMMA or PVP) structures ranged from 275.6 to 290.6 nm. These SEM images revealed that the BCP/polymer composites filled the voids in the $PC_{61}BM$ layer during the spin-coating process. Therefore, only a single layer containing $PC_{61}BM$ and the BCP/polymer composite appeared on the

Preprints (www.preprints.org) | NOT PEER-REVIEWED | Posted: 27 November 2020 doi:10.20944/preprints202011.0705.v1

surface of the $MAPbI_3$ layer. The good passivation of the BCP/polymer composite on the $PC_{61}BM$ layer would potentially facilitate electron transport from $PC_{61}BM$ to the cathode.

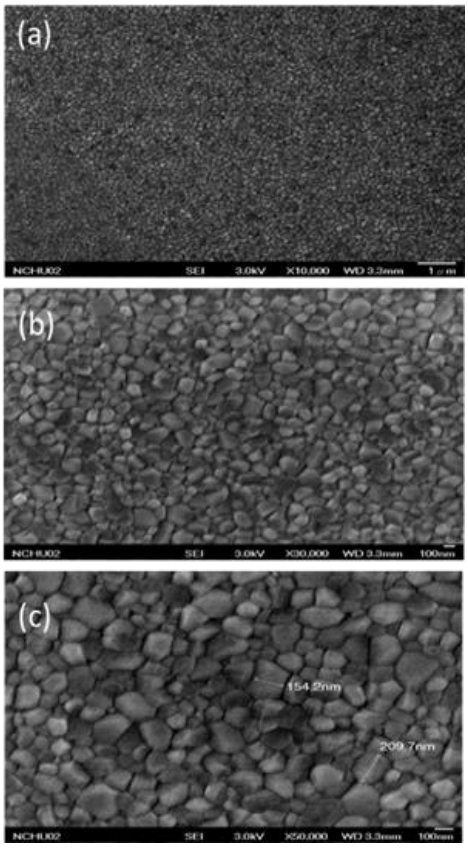

Figure 4. SEM images [(a) x10,000; (b) x30,000; (c) x50,000] of a $MAPbI_3$ perovskite film coated on the HTL, recorded after thermal annealing (80 °C, 5 min).

Preprints (www.preprints.org) | NOT PEER-REVIEWED | Posted: 27 November 2020 doi:10.20944/preprints202011.0705.v1

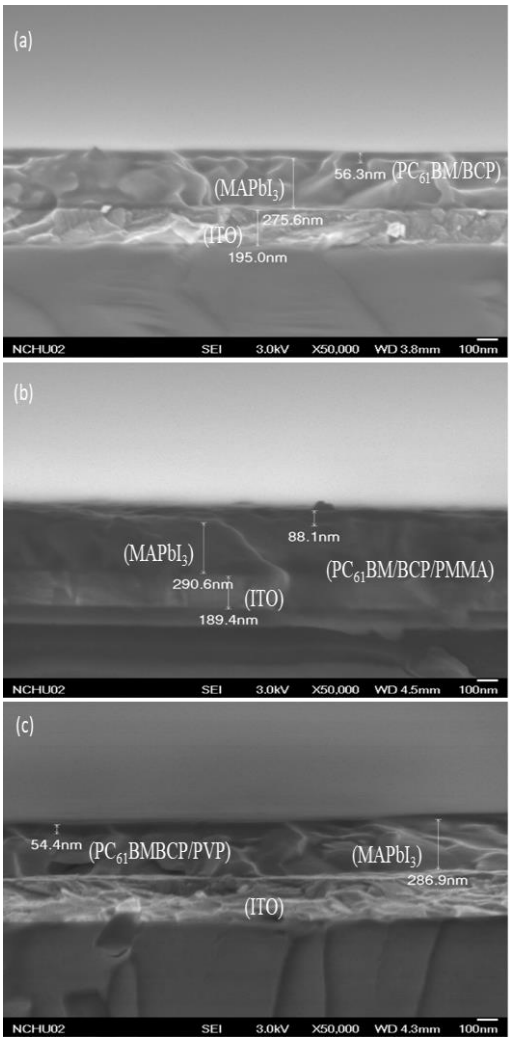

Figure 5. Cross-sectional SEM images of ITO/PEDOT:PSS/$MAPbI_3$/$PC_{61}BM$ structures coated with hole-blocking/electron-transporting interfacial layers of (a) BCP, (b) BCP/PMMA (5:1, w/w), and (c) BCP/PVP (5:1, w/w), recorded after thermal annealing (80 °C, 5 min).

3.4 XRD Images of $MAPbI_3$ Perovskite Films Coated with Various Hole-blocking/Electron-Transporting Interfacial Films

To investigate the effect of the hole-blocking/electron-transporting interfacial layers on the storage-stability of the $MAPbI_3$ film, we used XRD to study the crystal structures of the $MAPbI_3$ films after storage under ambient conditions for 10 days. Figure 6 presents the XRD patterns of the ITO/PEDOT:PSS/$MAPbI_3$/$PC_{61}BM$ structures coated

Preprints (www.preprints.org) | NOT PEER-REVIEWED | Posted: 27 November 2020 doi:10.20944/preprints202011.0705.v1

with electron-transporting interfacial layers of BCP, BCP/PMMA (5:1, w/w), and BCP/PVP (5:1, w/w). The patterns of the $MAPbI_3$ films featured diffraction peaks at 14.2, 28.4, and 31.6°, corresponding to the (110), (220), and (310) phases, respectively [45, 46], suggesting tetragonal perovskite structures having lattice constants *a* and *b* of 8.883 Å and *c* of 12.677 Å [45]. Figure 6(a) reveals that $MAPbI_3$ dissociated partially into MAI and PbI_2 after storage under the ambient conditions for 10 days, with a diffraction peak for PbI_2 appearing at 13° [45]. For the $MAPbI_3$ film coated with the BCP/PMMA blend film, the intensity of this diffraction peak at 13° was suppressed significantly relative to that of the $MAPbI_3$ coated with BCP [Figure 6(b)]. Thus, the addition of PMMA in the BCP layer inhibited the permeation of moisture into the $MAPbI_3$ layer to prevent its dissociation. In contrast, when compared with the $MAPbI_3$ film coated with the layer of BCP, the intensity of the PbI_2 diffraction peak at 13° was higher for the $MAPbI_3$ film coated with the BCP/PVP blend film after storage under ambient conditions for 5 and 10 days [Figure 6(c)]. Thus, the $MAPbI_3$ film coated with the BCP/PVP blend film was not resistant toward the permeation of moisture, suggesting poor compatibility between BCP and PVP.

Preprints (www.preprints.org) | NOT PEER-REVIEWED | Posted: 27 November 2020 doi:10.20944/preprints202011.0705.v1

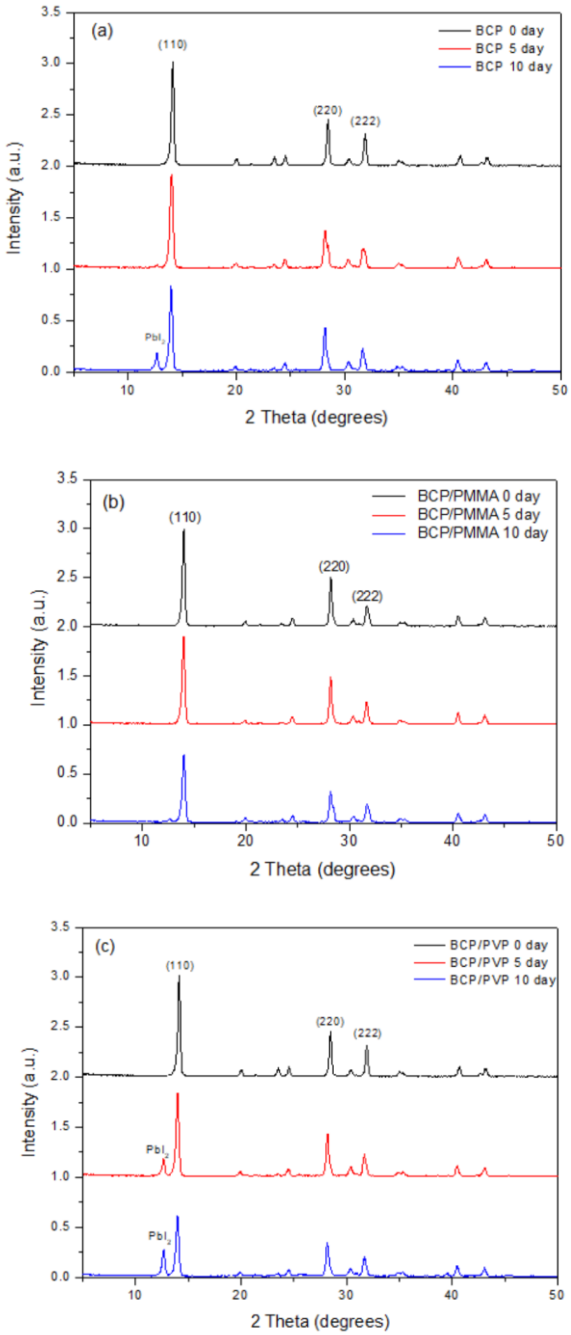

Figure 6. XRD patterns of ITO/PEDOT:PSS/$MAPbI_3$/$PC_{61}BM$ structures coated with hole-blocking/electron-transporting interfacial layers of (a) BCP, (b) BCP/PMMA (5:1, w/w), and (c) BCP/PVP (5:1, w/w), recorded after storage under ambient conditions for 0, 5, and 10 days.

Preprints (www.preprints.org) | NOT PEER-REVIEWED | Posted: 27 November 2020 doi:10.20944/preprints202011.0705.v1

3.5 AFM Images and CAs of BCP/PMMA and BCP/PVP Composite Films

We used AFM to study the surface morphologies of the BCP/PMMA and BCP/PVP hole-blocking/electron-transporting interfacial layers. Figures S2 and S3 display topographic and phase images of films of BCP and the BCP/PMMA and BCP/PVP composites, recorded after thermal treatment at 80 °C for 5 min. Table S1 summarizes the surface roughnesses of these BCP, BCP/PMMA, and BCP/PVP films. The topographic images in Figure S2 reveal that the surface roughness of the BCP films was not enhanced after the addition of PMMA. No phase separation was evident in the phase images of the composite films. Thus, BCP and PMMA exhibited good compatibility. In contrast, significant phase separation was evident in the phase images of the BCP/PVP composite films (Figure S3), suggesting poor compatibility between BCP and PVP. Nevertheless, the surface roughnesses of the BCP/PVP films were not higher than those of the BCP/PMMA films.

We also used AFM to determine the stability of the surface morphologies of the films of BCP and the BCP/PMMA, and BCP/PVP composites. Figures 7–9 display AFM images of the BCP, BCP/PMMA (5:1, w/w), and BCP/PVP (5:1, w/w) films, respectively, after storage under ambient condition for 0, 5, and 10 days. The morphology of BCP film was modified only slightly after storage for 5 days, but it changed significantly after 10 days (Figure 7). The morphology of the BCP/PMMA film (Figure 8) had changed only slightly after storage for 10 days, consistent with the good compatibility of BCP and PMMA. In other words, the BCP/PMMA film had high morphological stability. In contrast, the stability of the morphology of the BCP/PVP film was much poorer than those of the BCP film (Figure 9). Some of the BCP had separated from the BCP/PVP film, leading to the formation of BCP-based crystals after storage for 5 days, with a higher density appearing after storage for 10 days. Unlike the BCP and BCP/PMMA films, the surface roughness of the BCP/PVP

 doi:10.20944/preprints202011.0705.v1

film was enhanced significantly upon increasing the storage time under ambient conditions.

To examine the mechanism behind the morphological changes of the composite films under ambient conditions, we measured the hydrophobicity/hydrophilicity of the BCP/PMMA and BCP/PVP films using a CA meter. Figures S4 and S5 display photographs of water droplets on the BCP, BCP/PMMA and BCP/PVP films that had been stored under ambient condition for 0, 5, and 10 days. Table S1 lists the CAs of the BCP, BCP/PMMA and BCP/PVP films. Initially, the CA of the BCP film was 74.5°, suggesting low hydrophobicity; the CA decreased upon increasing the storage time, consistent with an increase in the permeation of moisture into this film and the significant change in the morphology of BCP film observed in Figure 7. The CA of the BCP film increased upon increasing the content of PMMA. Moreover, the CA of the BCP/PMMA (5:1, w/w) film did not decrease with increasing the storage time. The presence of the highly hydrophobic PMMA prevented the intrusion of moisture into the BCP film, consistent with the high morphological stability observed for the BCP/PMMA composite film in Figure 8. In contrast, the CA decreased upon increasing the PVP content in the BCP/PVP composite films. Furthermore, the CA of the BCP/PVP (5:1, w/w) film decreased significantly upon increasing the storage time. The presence of PVP, with low hydrophobicity, enhanced the permeation of moisture into the BCP film. As a result, phase separation of BCP and PVP occurred, promoting the formation of BCP-based crystals in the BCP/PVP film, as observed in Figure 9.

Preprints (www.preprints.org) | NOT PEER-REVIEWED | Posted: 27 November 2020 doi:10.20944/preprints202011.0705.v1

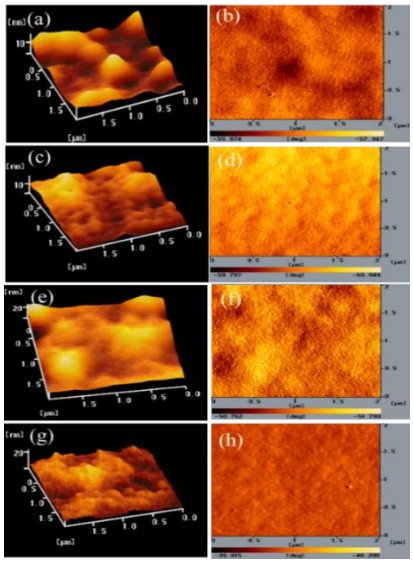

Figure S2. (a, c, e, g) Topographic and (b, d, f, h) phase AFM images of (a, b) BCP, (c, d) BCP/PMMA (10:1, w/w), (e, f) BCP/PMMA (5:1, w/w), and (g, h) BCP/PMMA (5:2, w/w) hole-blocking/electron-transporting interfacial layers, recorded after thermal treatment (80 °C, 5 min).

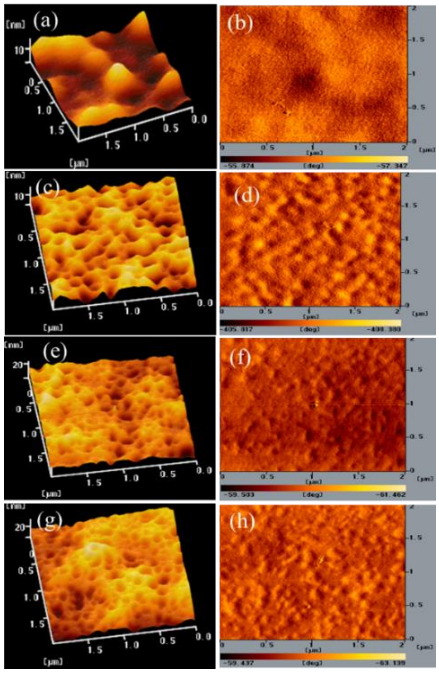

Figure S3. (a, c, e, g) Topographic and (b, d, f, h) phase AFM images of (a, b) BCP, (c, d) BCP/PVP (10:1, w/w), (e, f) BCP/PVP (5:1, w/w), and (g, h) BCP/PVP (5:2, w/w) hole-blocking/electron-transporting interfacial layers, recorded after thermal treatment (80 °C, 5 min).

Preprints (www.preprints.org) | NOT PEER-REVIEWED | Posted: 27 November 2020 doi:10.20944/preprints202011.0705.v1

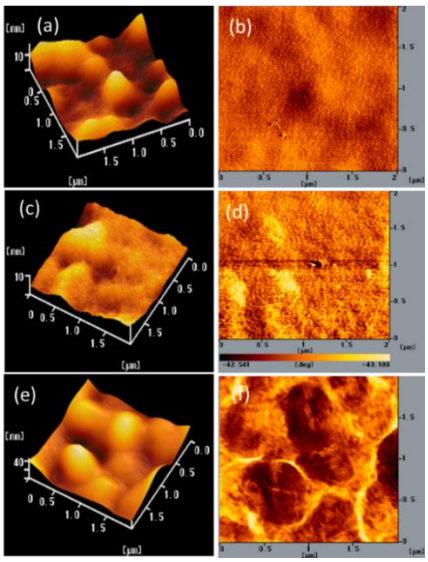

Figure 7. (a, c, e) Topographic and (b, d, f) phase AFM images of a BCP film after storage under ambient conditions for (a, b) 0, (c, d) 5, and (e, f) 10 days.

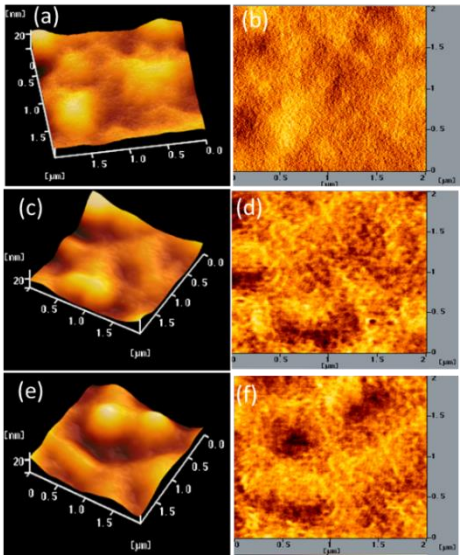

Figure 8. (a, c, e) Topographic and (b, d, f) phase AFM images of a BCP/PMMA (5:1, w/w) film after storage under ambient conditions for (a, b) 0, (c, d) 5, and (e, f) 10 days.

Preprints (www.preprints.org) | NOT PEER-REVIEWED | Posted: 27 November 2020 doi:10.20944/preprints202011.0705.v1

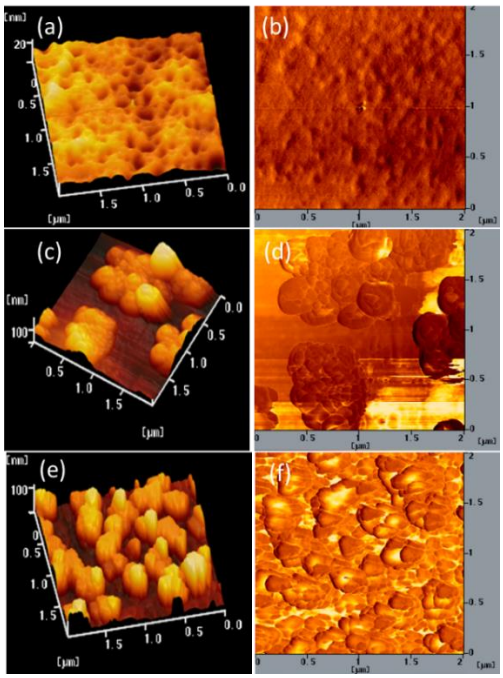

Figure 9. (a, c, e) Topographic and (b, d, f) phase AFM images of a BCP/PVP (5:1, w/w) film after storage under ambient conditions for (a, b) 0, (c, d) 5, and (e, f) 10 days.

Table S1. Surface roughnesses and CAs of films of BCP, BCP/PMMA, and BCP/PVP composites after storage under ambient conditions for 0, 5, and 10 days.

Sample	**Composition (w/w)**	**Time (days)**	**RMS (nm)**	CA (°)
I-1	BCP	0	3.27	74.5
I-2	BCP	5	2.76	49.0
I-3	BCP	10	7.55	37.8
II	BCP/PMMA (10:1)	0	3.25	75.5
III-1	BCP/PMMA (5:1)	0	3.18	78.4
III-2	BCP/PMMA (5:1)	5	5.14	74.4
III-3	BCP/PMMA (5:1)	10	5.31	72.3
IV	BCP/PMMA (5:2)	0	3.29	81.8
V	BCP/PVP (10:1)	0	3.12	58.4
VI-1	BCP/PVP (5:1)	0	3.09	53.5
VI-2	BCP/PVP (5:1)	5	26.45	43.9
VI-3	BCP/PVP (5:1)	10	38.32	35.7
VII	BCP/PVP (5:2)	0	3.15	43.0

Preprints (www.preprints.org) | NOT PEER-REVIEWED | Posted: 27 November 2020 doi:10.20944/preprints202011.0705.v1

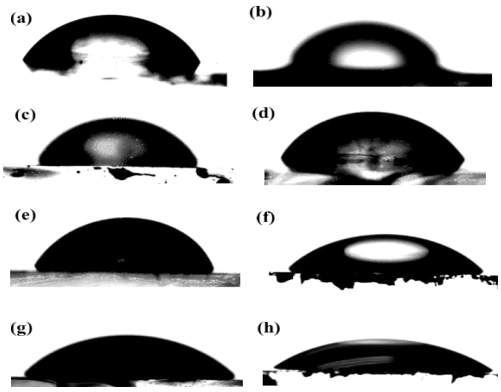

Figure S4. Photographs of water droplets on (a) BCP, (b) $PC_{61}BM$, (c, d, e) BCP/PMMA (10:1, 5:1, and 5:2, w/w), and (f, g, h) BCP/PVP (10:1, 5:1, and 5:2, w/w) films.

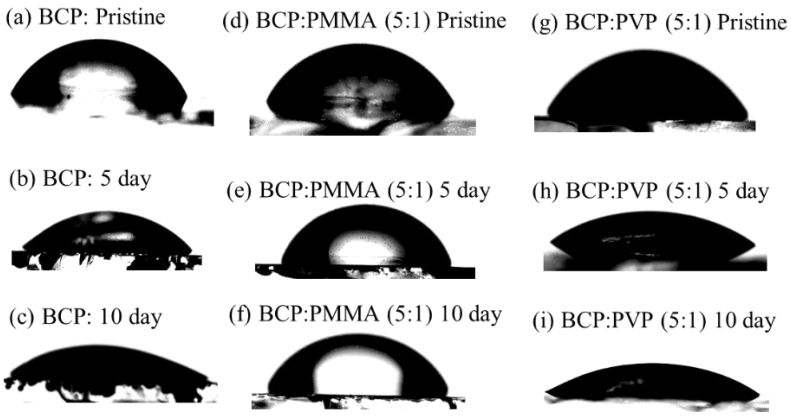

Figure S5. Photographs of water droplets on (a–c) BCP, (d–f) BCP/PMMA (5:1, w/w), and (g–i) BCP/PVP (5:1, w/w) films after storage under ambient conditions for 0, 5, and 10 days.

3.6 PV Characteristics

Figure 10 presents the photocurrent density–voltage plots of PVSCs featuring the BCP, BCP/PMMA, and BCP/PVP films as hole-blocking/electron-transporting interfacial layers. Table 1 summarizes the PV properties of these PVSCs. For PVSC I, prepared with BCP as the electron-transporting interfacial layer, a value of V_{OC} of 0.90 V, a value of J_{SC} of 21.2 mA cm^{-2}, an FF of 0.62, and a PCE of 11.78% were obtained.

Preprints (www.preprints.org) | NOT PEER-REVIEWED | Posted: 27 November 2020 doi:10.20944/preprints202011.0705.v1

Compared with the BCP-based PVSC, the values of V_{OC} and the FFs of the PVSCs incorporating the BCP/PMMA blend films (PVSCs II–IV) did not change significantly upon varying the PMMA content; the values of J_{SC} and the PCEs did, however, decrease slightly upon increasing the PMMA content, consistent with the lower BCP content in the electron-transporting interfacial layer. Decreasing the BCP content inhibited electron transport from the $MAPbI_3$ layer to the cathode. The lowest values of J_{SC} and PCE were those of PVSC IV incorporating 40 wt.% PMMA. In contrast, the values of V_{OC}, J_{SC}, and PCE of the PVSCs incorporating BCP/PVP blend films (PVSCs V–VII) increased upon increasing the PVP content, and were greater than those of the BCP-based PVSC. The highest values of V_{OC} (0.92 V), J_{SC} (21.72 mA cm^{-2}), FF (0.62), and PCE (12.41 %) were obtained for PVSC VI, prepared with BCP/PVP (5:1, w/w) as the hole-blocking/electron-transporting interfacial layer. The presence of PVP at the interface between $PC_{61}BM$ and the cathode might have induced the formation of a dipole layer, thereby enhancing the built-in potential across the cell and facilitating electron transport from the perovskite layer to the cathode [45]. As a result, the PV properties of the BCP/PVP-based PVSCs were enhanced. Nevertheless, a larger PVP content in the BCP/PVP blend film did not improve the PV properties of PVSC VII, which provided a PCE lower than that of PVSC I. The poor compatibility of BCP and PVP would inhibit electron transport from $PC_{61}BM$ to the cathode. Consequently, the PV performance of the BCP/PVP (5:2, w/w)–based PVSC VII was poor.

Preprints (www.preprints.org) | NOT PEER-REVIEWED | Posted: 27 November 2020 doi:10.20944/preprints202011.0705.v1

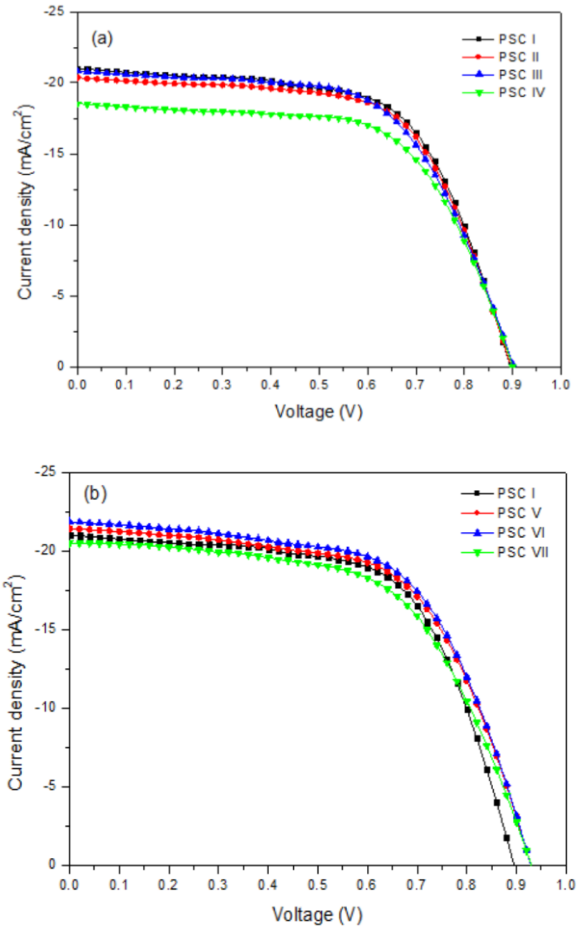

Figure 10. Current density–potential plots of PVSCs incorporating BCP, BCP/PMMA, and BCP/PVP films, illuminated under AM 1.5G light at 100 mW cm^{-2}.

Table 1. PV properties of PVSCs incorporating BCP, BCP/PMMA, and BCP/PVP films

PVSC	Electron-transporting layer	Composition (w/w)	V_{OC} (V)	J_{SC} (mA cm^{-2})	FF	PCE (%)
PVSC-I	BCP	0.0	0.90	21.20	0.62	11.78
PVSC-II	BCP/PMMA	10:1	0.90	20.70	0.62	11.61
PVSC-III	BCP/PMMA	5:1	0.90	20.94	0.61	11.56
PVSC-IV	BCP/PMMA	5:2	0.90	18.50	0.64	10.66
PVSC-V	BCP/PVP	10:1	0.92	21.35	0.62	12.07
PVSC-VI	BCP/PVP	5:1	0.92	21.72	0.62	12.41
PVSC-VII	BCP/PVP	5:2	0.93	20.46	0.62	11.70

Preprints (www.preprints.org) | NOT PEER-REVIEWED | Posted: 27 November 2020 doi:10.20944/preprints202011.0705.v1

Figure 11 displays the external quantum efficiency (EQE) spectra of the PVSCs incorporating films of BCP, BCP/PMMA, and BCP/PVP. Similar EQE profiles of $MAPbI_3$-based PVSCs have been reported several times previously [11, 47, 48]. The partial photoresponse near 400 nm arose from the absorption of $PC_{61}BM$ [49]. Relative to the BCP-based PVSC I, the EQEs decreased upon increasing the amount of PMMA in the BCP/PMMA-based PVSC-II, PVSC-III, and PVSC-IV. A greater PMMA content in the BCP/PMMA blend film inhibited the transport of electrons from the $MAPbI_3$ layer to the cathode. As a result, the EQEs decreased when the PVSCs had higher PMMA contents. In contrast, the EQEs of the BCP/PVP-based PVSC V, PVSC-VI, and PVSC-VII were greater than those of the BCP-based PVSC I. The presence of PVP at the interface between the $PC_{61}BM$ layer and the cathode might have promoted the transport of electrons from the $PC_{61}BM$ layer to the cathode. Nevertheless, a larger PVP content in the BCP/PVP blend film did not enhance the EQE of PVSC VII—it was lower than that of PVSC I.

Preprints (www.preprints.org) | NOT PEER-REVIEWED | Posted: 27 November 2020 doi:10.20944/preprints202011.0705.v1

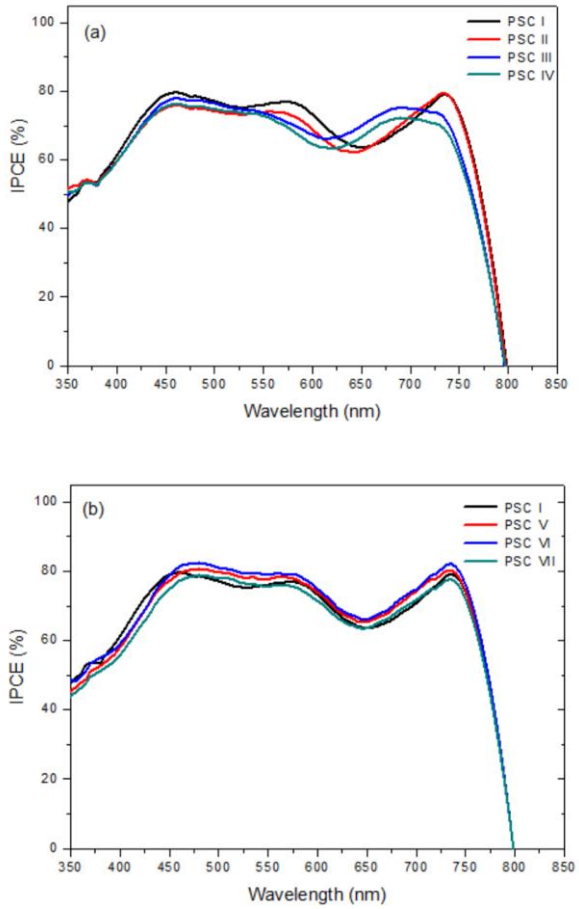

Figure 11. EQE spectra of PVSCs incorporating films of BCP, BCP/PMMA, and BCP/PVP, recorded under monochromatic irradiation.

Figure 12 reveals the storage stabilities under ambient condition of the PVSCs incorporating BCP, BCP/PMMA, and BCP/PVP. The PCE-stabilities of the BCP/PMMA-based PVSC II and PVSC III were superior to that of the BCP-based PVSC-I. Higher PCE-stabilities were observed for the BCP/PMMA-based PVSCs upon increasing their PMMA content, consistent with the higher hydrophobicity of PMMA preventing moisture from entering the BCP film. Nevertheless, the PCE-stability of PVSC IV was lower than those of PVSC II and PVSC III, presumably because of the poorer PV properties of PVSC IV with its higher PMMA content. In contrast, the PCE-stabilities of the BCP/PVP-based PVSCs were poorer than that of the

Preprints (www.preprints.org) | NOT PEER-REVIEWED | Posted: 27 November 2020 doi:10.20944/preprints202011.0705.v1

BCP-based PVSC-I, with lower PCE-stability observed upon increasing the PVP content. The phase separation of BCP and PVP, and the high hydrophilicity of PVP, promoted the intrusion of moisture into the BCP film. Consequently, the PVSCs incorporating the BCP/PVP composite film exhibited poor PCE-stability.

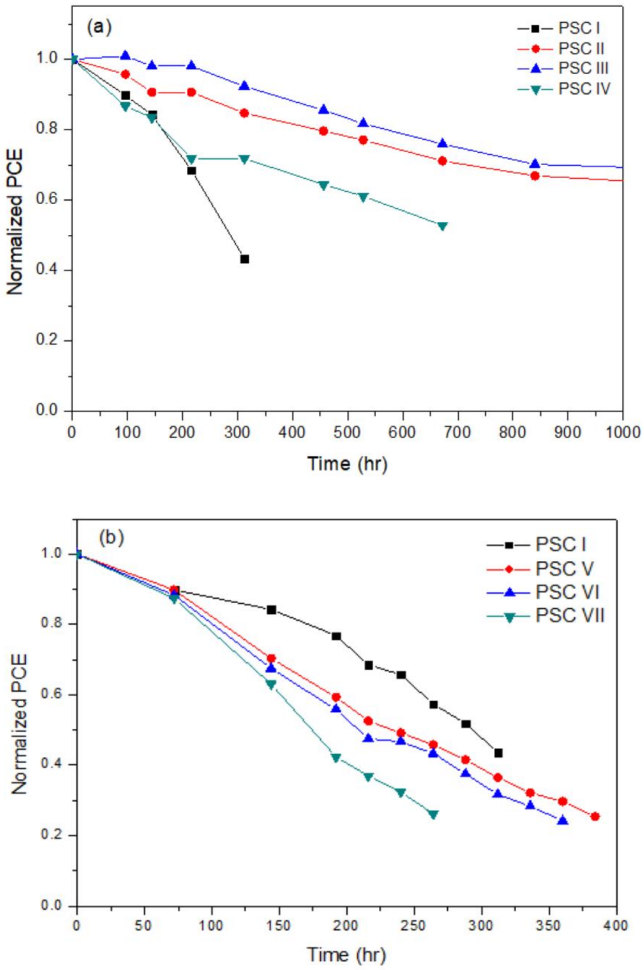

Figure 12. Storage-stability under ambient conditions of PVSCs incorporating BCP, BCP/PMMA, and BCP/PVP.

 doi:10.20944/preprints202011.0705.v1

Conclusion

The PV properties and stabilities of $MAPbI_3$-based PVSCs incorporating BCP/PMMA and BCP/PVP films as hole-blocking/electron-transporting interfacial layers have been studied. The storage-stability of the BCP/PMMA-based PVSCs was enhanced significantly relative to that of the BCP-based PVSC, but the PV performance decreased slightly after the incorporation of PMMA. The improved storage-stability arose from the greater hydrophobicity and moisture-resistance of the resulting BCP/PMMA layer. A higher content of PMMA in the BCP layer inhibited charge transfer from the $MAPbI_3$ layer to the cathode, resulting in a lower short-circuit current density and a less efficient PVSC. In contrast, the PV performance of BCP/PVP-based PVSCs was enhanced relative to that of the BCP-based PVSC, but their storage-stability was poor. The presence of PVP promoted the electron-transporting across the BCP-based interfacial layer to cathode and resulted in PVSCs having higher current densities and PCEs. Nevertheless, poor compatibility between PVP and BCP resulted in the BCP/PVP-based PVSCs displaying poor storage-stability.

Acknowledgment

We thank the Ministry of Science and Technology of Taiwan (MOST 109-2221-E-005-070) for financial support.

References

1. Kim, J.Y.; Lee, J.W.; Jung, H.S.; Shin, H.; Park, N.G. High-efficiency perovskite solar cells. *Chem. Rev.* **2020**, *120*, 7867–7918.
2. Xing, G. ; Mathews, N.; Sun, S.; Lim, S. S. ; Lim, Y.M. ; Gratzel, M. ; Mhaisalkar, S.; Sum, T.C. Long-range balanced electron- and hole-transport lengths in organic-inorganic $CH_3NH_3PbI_3$. Science **2013**,*342* ,344–347.

3. Li, S.; Ren, H.; Yan, Y. Boosting efficiency of planar heterojunction perovskite solar cells to 21.22 % by a facial two step deposition strategy. Appl. Surf. Sci. **2019** ,*484* ,1191-1197.
4. Stranks, S.D.; Eperon, G.E.; Grancini, G.; Menelaou, C.; Alcocer, M. J. P.; Leijtens,T.; Herz, L. M.; Petrozza, A.; Snaith, H. J. Electron-hole diffusion lengths exceeding 1 micrometer in an organometal trihalide perovskite absorber. Science **2013,***342***,**341–344.
5. Dong, Q.; Fang, Y.; Shao, Y.; Mulligan, P.; Qiu, J.; Cao, L.; Huang, J. Electron-hole diffusion lengths >175 m in solution grown $CH_3NH_3PbI_3$ single crystals, Science **2015,** *347***,** 967–970.
6. Kojima, A.; Teshima, K.; Shirai, Y.; Miyasaka, T. Organometal halide perovskites as visible-light sensitizers for photovoltaic cells, J. Am. Chem. Soc. **2009**,*131*, 6050–6051.
7. Docampo, P.; Ball, J.M.; Darwich, M.; Eperon, G.E.; Snaith, H.J. Efficient organometal trihalide perovskite planar-heterojunction solar cells on flexible polymer substrates, Nat. Commun. **2013,***4*, 2761.
8. Song, Z.; Watthage, S.C.; Phillips, A.B.; Heben, M.J. Pathways toward high-performance perovskite solar cells: Review of recent advances in organo-metal halide perovskites for photovoltaic applications, J. Photon. Energy **2016**, *6* ,022001.
9. Gao, B.; Meng J. RbCs(MAFA)PbI_3 perovskite solar cell with 22.81% efficiency using the precise ions cascade regulation, Appl. Surface Sci. **2020**, *530* ,147240.
10. Saliba, M.; Matsui, T.; Seo, J.; Domanski, K.; Baena, J. P. C.; Nazeeruddin, M. K.; Zakeeruddin, S. M.; Tress, W.; Abate, A.; Hagfeldtd, A.; Gratzel, M. Cesium-

 doi:10.20944/preprints202011.0705.v1

containing triple cation perovskite solar cells: Improved stability, reproducibility and high efficiency, Energy Environ. Sci. **2016**, *9* ,1989.

11. Chen, W.; Xu, L.; Feng, X.; Jie, J.; He, Z. Metal acetylacetonate series in interface engineering for full low-temperature-processed, high-performance, and stable planar perovskite solar cells with conversion efficiency over 16% on 1 cm^2 scale, Adv. Mater. **2017**, *29*, 1603923.
12. Ghoreishi, F. S.; Ahmadi, V.; Poursalehi, R.; Pour, M. S.; Johansson, M. B.; Boschloo, G.; Johansson, E.M.J. Enhanced performance of $CH_3NH_3PbI_3$ perovskite solar cells via interface modification using phenyl ammonium iodide derivatives, J. Power Sources. **2020**,*473*, 228492.
13. Li, D.; Chao, L.; Chen, C.; Ran, X.; Wang, Y.; Niu, T.; Lv, S.; Wu, H.; Xia, Y. Ran, C.; Song, L.; Chen, S.; Chen, Y.; Huang, W. In situ interface engineering for highly efficient electron-transport layer-free perovskite solar cells, Nano Lett. **2020**,*20*,5799–5806.
14. Girolamo, D. D.; Giacomo, F.D.; Matteocci, F.; Marrani, A.G.; Dini, D.; Abate, A.Progress, highlights and perspectives on NiO in perovskite photovoltaics, Chem. Sci. **2020**, *11*,7746–7759.
15. Kong J.; Wang, H. Röhr, J. A.; Fishman, Z. S.; Zhou, Y.; Li, M.; Cotlet, M.; Kim, G.; Karpovich, C.; Antonio, F.; Padture, N.P.; Taylor, A. D. Perovskite solar cells with enhanced fill factors using polymer capped solvent annealing, ACS Appl. Energy Mater. **2020**, *3*, 7231–7238.
16. Kuo, D. W.; Liu, G. Z.; Lee, R.H. Star-shaped molecule with planar triazine core and perylene diimide branches as an n-type additive for bulk-heterojunction perovskite solar cells, Dyes Pigments **2019**, *170*, 107562.
17. Chu, H.Y.; Hong, J. Y.; Huang, C. F.; Wu, J. Y.; Wang, T. L.; Wu, T. M.; Lee, R.H. Enhanced photovoltaic properties of perovskite solar cells by the addition of

 doi:10.20944/preprints202011.0705.v1

cellulose derivatives to $MAPbI_3$ based photoactive layer, Cellulose **2019**,*26*, 9229–9239.

18. Guo, Y. L.; Shoyama, K.; Sato, W.; Nakamura, E. Polymer stabilization of lead(II) perovskite cubic nanocrystals for semitransparent solar cells, Adv. Energy Mater. **2016**,*6*, 1502317.
19. Liu, C.; Huang, Z.; Hu, X.; Meng, X.; Huang, L.; Xiong, J.; Tan, L.; Chen, Y. Grain boundary modification via F4-TCNQ to reduce defects of perovskite solar cells with excellent device performance, ACS Appl. Mater. Interfaces **2018**,*10*,1909–1916.
20. Huang, Z.Q.; Hu, X. T.; Liu, C.; Tan, L.C.; Chen, Y. W. Nucleation and crystallization control via polyurethane to enhance the bendability of perovskite solar cells with excellent device performance, Adv. Funct. Mater. **2017**,*27*, 1703061.
21. Yang, Y.; Song, J.; Zhao, Y. L.; Zhu, L.; Gu, X.Q.; Gu, Y.Q.; Che, M.; Qiang, Y. H. Ammonium-iodide-salt additives induced photovoltaic performance enhancement in one-step solution process for perovskite solar cells. J. Alloy. Compd. **2016**, *684*, 84–90.
22. Zhu, T.; Liu, D. Zheng, J.; Coolen, L.; Pauporte, T. PEAI-based interfacial layer for high-efficiency and stable solar cells based on a MACl-mediated grown $FA_{0.94}MA_{0.06}PbI_3$ perovskite, ACS Appl. Mater. Interfaces **2020**,*12*, 37197–37207.
23. Saliba, M.; Matsui, T.; Domanski, K.; Seo, J.Y.; Ummadisingu, A.; Zakeeruddin, S.M.; Baena, J.P.C.; Tress, W.R.; Abate, A.; Hagfeldt, A.; Grätzel, M. Incorporation of rubidium cations into perovskite solar cells improves photovoltaic performance, Science **2016**, *354*,206–209.

 doi:10.20944/preprints202011.0705.v1

24. Chai, L.; Zhong, M.; Li, X.; Wu, N.; Zhou, J. The effect of bromine doping on the perovskite solar cells modified by PVP/PEG polymer blends, Superlattice. Microst. **2018**, *120*, 279–287.
25. Chang, C.Y.; Chu, C.Y.; Huang, Y.C.; Huang, C.W.; Chang, S.Y.; Chen, C. A.; Chao, C. Y.; Su, W.F. Tuning perovskite morphology by polymer additive for high efficiency solar cell, ACS Appl. Mater. Interfaces 7 **2015**,*7*, 4955–4961.
26. Li, F.; Liu, M.Recent efficient strategies for improving the moisture stability of perovskite solar cells, J. Mater. Chem. A **2017**,*5*, 15447–15459.
27. Chen, W.; Wu, Y. Z.; Yue,Y. F.; Liu, J.; Zhang, W. J.; Yang, X. D.; Chen, H.; Bi, E. B.; Ashraful, I.; Gratzel, M.; L. Han, Y. Science **2015**,*350*, 944–948.
28. Zhu, Z.; Bai, Y.; Liu, X.; Chueh, C.-C.; Yang, S.; A. K. Y. Jen, Adv. Mater. **2016**,*28*, 6478–6484.
29. Hwang, I.; Jeong, I.; Lee, J.; Ko, M. J.; Yong, K. Enhancing stability of perovskite solar cells to moisture by the facile hydrophobic passivation, ACS Appl. Mater. Interfaces **2015**,*7*, 17330–17336.
30. Babu, V.; Pineda, R. F.; Ahmad, T.; Alvarez, A. O.; Castriotta, L. A.; Carlo, A. D.; Santiago, F. F.; Wojciechowski, K.; Improved stability of inverted and flexible perovskite solar cells with carbon electrode, ACS Appl. Energy Mater. **2020**,*3*,5126–5134.
31. Kundu, S.; Kelly, T. L.; Improving the moisture stability of perovskite solar cells by using PMMA/P3HT based hole-transport layers, Mater. Chem. Front. **2018**,*2*, 81–89.
32. Habisreutinger, S. N.; Leijtens, T.; Eperon, G. E.; Stranks, S. D.; Nicholas, R. J.; Snaith, H.J.Carbon nanotube/polymer composites as a highly stable hole collection layer in perovskite solar cells, Nano Lett. **2014**,*14*,5561–5568.

 doi:10.20944/preprints202011.0705.v1

33. Wu, C.; Li, H.; Yan, Y.; Chi, B.; Felice, K. M.; Moore, R. B.; Magill, B. A.; Mudiyanselage, R. R. H. H.; Khodaparast, G. A.; Sanghadasa, M.; Priya, S. Highly-stable organo-lead halide perovskites synthesized through green self-assembly process, Sol. RRL **2018**,*2*, 1800052.

34. Zhou, P.; Fang, Z.; Zhou, W.; Qiao, Q.; Wang, M.; Chen, Tao.; Yang, S.; Nonconjugated polymer poly(vinylpyrrolidone) as an efficient interlayer promoting electron transport for perovskite solar cells, ACS Appl. Mater. Interfaces **2017**,*9*, 32957–32964.

35. Li, B.; Zhang, Y.; Fu, L.; Yu, T.; Zhou, S.; Zhang, L.; Yin, L.; Surface passivation engineering strategy to fully-inorganic cubic $CsPbI_3$ perovskites for high-performance solar cells, Nat. Commun. **2018**,*9*,1076.

36. Zhang, Y.; Zhuang, X.; Zhou, K.; Cai, C.; Hu, Z.; Zhang, J.; Zhu, Y. Amorphous polymer with C=O to improve the performance of perovskite solar cells, J. Mater. Chem. C **2017**,*5*,9037–9043.

37. Ding, Y.; Yao, X.; Zhang, X.; Wei, C.; Zhao, Y.Surfactant enhanced surface coverage of $CH_3NH_3PbI_{3-x}Cl_x$ perovskite for highly efficient mesoscopic solar cells, J. Power Sources **2014**,*272*, 351–355.

38. Manshor, N. A.; Wali Q.; Wong, K. K.; Muzakir, S. K.; Fakharuddin, A.; Mende, L. S.; Jose, R. Humidity versus photo-stability of metal halide perovskite films in a polymer matrix, Phys. Chem. Chem. Phys. **2016**,*18*, 21629–21639.

39. Xiong, H.; DeLuca, G.; Rui, Y.; Zhang, B.; Li, Y.; Zhang, Q.; Wang, H.; Reichmanis, E.Modifying perovskite films with polyvinylpyrrolidone for ambient-air-stable highly bendable solar cells, ACS Appl. Mater. Interfaces **2018**,*10*, 35385–35394.

40. Chen, C.; Zhang, S.; Wu, S.; Zhang, W.; Zhu, H.; Xiong, Z.; Zhang, Y.; Chen, W. Effect of BCP buffer layer on eliminating charge accumulation for high

 doi:10.20944/preprints202011.0705.v1

performance of inverted perovskite solar cells, RSC Adv. **2017**,*7*, 35819-35826.

41. Butscher, J. F.; Intorp, S.; Kress, J.; An, Q.; Hofstetter, Y. J.; Hippchen, N.; Paulus, F.; Bunz, U. H. F.; Tessler, N.; Vaynzof, Y. Enhancing the open-circuit voltage of perovskite solar cells by embedding molecular dipoles within their hole-blocking layer, ACS Appl. Mater. Interfaces **2020**,*12,* 3572–3579.
42. Wang, Y.; Zhang, J.; Wu, Y.; Yi, Z.; Chi,F.; Wang H.; Li, W.; Zhang, Y.; Zhang, X.; Liu ,L.Solution-processed bathocuproine cathode buffer layer towards efficient planar heterojunction perovskite solar cells, Semicond. Sci. Technol. **2019**,*34*, 075023.
43. Luo, D.; Zhao, L.; Wu, J.; Hu, Q.; Zhang, Y.; Xu, Z.; Liu, Y.; Liu, T.; Chen, K.; Yang, W.; Zhang, W.; Zhu, R.; Gong, Q. Dual-source precursor approach for highly efficient inverted planar heterojunction perovskite solar cells, Adv. Mater. **2017**,*29*, 1604758.
44. Zhao, D.; Zhu, Z.; Kuo, M.Y.; Chueh, C.C.; Jen, A.K.Y. Hexaazatrinaphthylene derivatives: Efficient electron-transporting materials with tunable energy levels for inverted perovskite solar cells, Angew. Chem. Int. Ed. **2016**,*55*,8999–9003.
45. Xue, Q.; Hu, Z.; Sun, C.; Chen, Z.; Huang, F.; Yip, H. L.; Cao, Y. Metallohalide perovskite–polymer composite film for hybrid planar heterojunction solar cells, RSC Adv.**2015**,*5*,775–783.
46. Xiao, M.; Huang, F.; Huang, W.; Dkhissi, Y.; Zhu, Y.; Etheridge, J.; Weale, A.G. Bach, U.; Cheng, Y. B.; Spiccia, L. A fast deposition-crystallization procedure for highly efficient lead iodide perovskite thin-film solar cells, Angew. Chem. **2014**,*126*,10056–10061.
47. Karuppuswamy, P.; Hanmandluc, C.; Boopathic, K. M.; Perumale, P.; Liu, C.C.; Chen, Y. F.; Chang, Y. C.; Wang, P.; Lai, C. C. S.; Chu, C. W. Solution-processable

 doi:10.20944/preprints202011.0705.v1

electron transport layer for efficient hybrid perovskite solar cells beyond fullerenes, Sol. Energy Mater. Sol. Cells **2017**,*169*,78–85.

48. Zuo, L.; Guo, H.; deQuilettes, D. W.; Jariwala, S.; Marco, N. D.; Dong, S.; DeBlock, R.; Ginger, D. S.; Dunn, B.; Wang, M.; Yang, Y. Polymer-modified halide perovskite films for efficient and stable planar heterojunction solar cells, Sci. Adv. **2017**,*3*, e1700106.
49. Jin, Z. W.; Wang, J. H. A trilayer architecture for polymer photoconductors, Appl. Phys. Lett. **2013**,*102*, 053304.